JACS
JOURNAL OF THE AMERICAN CHEMICAL SOCIETY
Article
pubs.acs.org/JACS

Deciphering Halogen Competition in Organometallic Halide Perovskite Growth

Bin Yang,[†] Jong Keum,[†,‡] Olga S. Ovchinnikova,[†,#] Alex Belianinov,[†,#] Shiyou Chen,[∥] Mao-Hua Du,[§] Ilia N. Ivanov,[†] Christopher M. Rouleau,[†] David B. Geohegan,[†] and Kai Xiao*[,†]

[†]Center for Nanophase Materials Sciences, [‡]Neutron Sciences Directorate, [#]Institute for Functional Imaging of Materials, and [§]Materials Science & Technology Division, Oak Ridge National Laboratory, Oak Ridge, Tennessee 37831, United States
[∥]Key Laboratory of Polar Materials and Devices (MOE), East China Normal University, Shanghai 200241, China

Supporting Information

ABSTRACT: Organometallic halide perovskites (OHPs) hold great promise for next-generation, low-cost optoelectronic devices. During the chemical synthesis and crystallization of OHP thin films, a major unresolved question is the competition between multiple halide species (e.g., I^-, Cl^-, Br^-) in the formation of the mixed-halide perovskite crystals. Whether Cl^- ions are successfully incorporated into the perovskite crystal structure or, alternatively, where they are located is not yet fully understood. Here, in situ X-ray diffraction measurements of crystallization dynamics are combined with ex situ TOF-SIMS chemical analysis to reveal that Br^- or Cl^- ions can promote crystal growth, yet reactive I^- ions prevent them from incorporating into the lattice of the final perovskite crystal structure. The Cl^- ions are located in the grain boundaries of the perovskite films. These findings significantly advance our understanding of the role of halogens during synthesis of hybrid perovskites and provide an insightful guidance to the engineering of high-quality perovskite films, essential for exploring superior-performing and cost-effective optoelectronic devices.

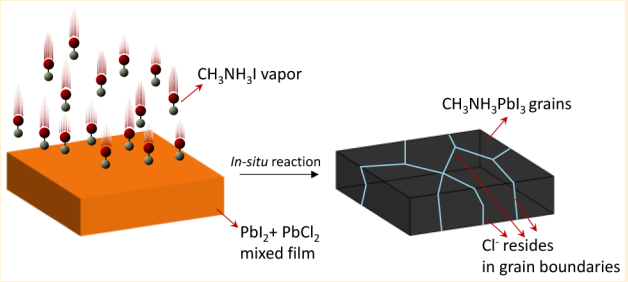

1. INTRODUCTION

Organometallic halide perovskites (OHPs) are rapidly emerging as a promising class of materials for high-performance and cost-effective optoelectronic devices, including solar cells,[1] light-emitting diodes,[2] X-ray sensors,[3] and UV−visible photodetectors.[4] Their superior optoelectronic properties include strong optical absorption,[5] broadly tunable optical band gaps,[6] long carrier diffusion lengths (≥1 μm),[7] and high carrier mobilities (≥10 $cm^2/V{\cdot}s$).[7a,b] The OHPs can be classified into two categories, depending on the halogen composition in the OHP molecules: pure halide perovskite (*p*HP) with single halogen species, e.g., methylammonium lead iodide ($CH_3NH_3PbI_3$)[1a] and formamidinium lead iodide,[1b,d] and mixed-halide perovskites (*m*HP) with multiple halogen species, e.g., $CH_3NH_3PbI_{3-x}Cl_x$,[1c] $CH_3NH_3PbI_{3-x}Br_x$,[8] and $(NH_2)_2CHPbI_{3-x}Br_x$.[1b,d] Compared to the *p*HPs, the *m*HPs have attracted more research interest due to the broader range of tunability of their optoelectronic properties.[1d,6,9] For example, a certain fractional substitution of Br^- for I^- in $CH_3NH_3PbI_3$ leads to widely tunable optical band gaps and light absorption capabilities for (I, Br) *m*HPs.[6] In the case of (I, Cl) *m*HPs, the addition of Cl^- significantly enhances carrier diffusion lengths in triiodide perovskites from 100 nm to 1 μm.[7c] However, previous studies have showed that the Cl^- was not found in the unit cell (or may be in a nondetectable level due to instrument limit of detection).[10] Despite these insightful findings, there was still no direct and clear evidence to identify where the Cl^- goes. Whether the Cl^- is doped into the triiodide perovskite crystal structure or where the Cl^- resides is still under intensive debate.[10c,11] Resolving this structure−functionality relationship is of both technological and fundamental importance, requiring elucidation of the different chemical reactions and kinetics that occur during the synthesis of (I, Cl) *m*HPs. However, the crystallization kinetics of the perovskite films was rarely studied. Moreover, maximizing the performance and reproducibility of OHP-based optoelectronic devices requires establishing the optimization of controllable film growth processes for high-quality perovskite films with large grains and low defect density.[12] At the root of this major challenge is the lack of understanding of the underlying mechanisms that govern crystal nucleation and growth during the complex chemical reactions responsible for the synthesis of OHP films.

In this paper, we report the crystal growth kinetics of *p*HP triiodide perovskites by time-resolved in situ X-ray diffraction (XRD), revealing a diffusion-controlled, one-dimensional growth behavior. These isothermal in situ XRD measurements allowed the kinetics of chemical reactions between methylammonium iodide (CH_3NH_3I) molecules and mixed lead halide precursors to reveal the competition of halogens during the synthesis of perovskites. It was uncovered that in the

Received: December 18, 2015
Published: March 1, 2016

DOI: 10.1021/jacs.5b13254
J. Am. Chem. Soc. 2016, 138, 5028−5035

presence of reactive I^- ions neither Br^- nor Cl^- is incorporated into the final perovskite crystal structure; however, their presence can promote crystal growth. Time-of-flight secondary ion mass spectrometry (TOF-SIMS) measurements were used to directly map the element distribution of Cl^- and indicate the Cl^- was dispersed in the grain boundaries of perovskite films. These findings significantly advance our understanding of the role of halogens during synthesis of hybrid perovskites and provide an insightful and applicable guidance to the engineering of large-grain perovskite films for exploring superior-performing and cost-effective optoelectronic devices.

2. EXPERIMENTAL SECTION

2.1. Solar Cell Fabrication and Characterization. The lead(II) iodide (PbI_2, purchased from Sigma-Aldrich, use as received) was dissolved in dimethylformamide (DMF) solvent to make a solution with a concentration of 550 mg/mL. For the (I, Br)-based mixed-halide solution, the mole ratio between PbI_2 and lead(II) bromide ($PbBr_2$, purchased from Sigma-Aldrich, used as received) was 1:1 and the mixed powder was dissolved in DMF to make a solution concentration of 550 mg/mL. As for the (I, Cl)-based mixed-halide solution, the mole ratio between PbI_2 and lead(II) chloride ($PbCl_2$, purchased from Sigma-Aldrich, used as received) was 1:1 and the mixed powder was dissolved in the dimethyl sulfoxide (DMSO) solvent to make a solution concentration of 550 mg/mL. In order to completely dissolve the pure PbI_2, the solution was stirred and heated on a hot plate to 100 °C for ∼5 min. All the lead halide precursor films for in situ XRD studies were grown on glass substrates by spin-coating at 6000 rpm for 30 s in a N_2-filled glovebox.

Following spin-coating, the samples were heated at 100 °C for ∼1 min to eliminate residual solvent. Subsequently, CH_3NH_3I powder (purchased from 1-Material Inc., used as received) was dispersed around the cooled PbI_2 film on a hot plate. The sample was covered with a glass container and annealed at 160 °C for 30 min to produce visibly dark perovskite films. The titanium dioxide (TiO_2) layer was fabricated following the procedure reported previously.[12c] 2,2′,7,7-tetrakis[*N*,*N*-di(*p*-methoxyphenylamine)]-9,9-spirobifluorene (Spiro-OMeTAD, purchased from 1-Material Inc., used as received) solution (90 mg/mL in chlorobenzene) was doped by adding 10 μL of 4-*tert*-butylpyridine (tBP) and 45 μL of lithium bis(trifluoromethane sulfonyl) imide (Li-TFSI, 170 mg/mL in anhydrous acetonitrile), and then the mixture was spin-coated onto the film at 2000 rpm for 40 s. After leaving the sample in a desiccator for 24 h, 100-nm-thick silver (Ag) contacts were then formed by thermal evaporation at deposition rate of 1 Å/s at 10^{-6} mbar. The active area of the device was ∼7.5 mm^2, which was carefully measured and calculated by optical microscopy. The current density−voltage (J−V) curves were measured using a Keithley 2400 source meter in a N_2-filled glovebox. The devices were illuminated at 100 mW/cm^2 (AM 1.5 G solar spectrum) with a solar simulator (Radiant Source Technology, 300 W, Class A). Prior to each measurement, the light intensity was carefully calibrated using a NIST-certified Si-reference cell. The J−V curves were obtained by scanning in two modes: from reverse bias (−0.2 V) to forward bias (1.2 V) and then from forward bias (1.2 V) to reverse bias (−0.2 V), with a 50 ms sweep delay time.

2.2. In Situ X-ray Diffraction. The XRD patterns were collected using an X-ray diffractometer (PANAlytical X'Pert MPD Pro) with Cu Kα radiation (λ = 1.540 50 Å) equipped with an Anton Paar XRK-90 detector. The step size and scan rate for each measurement was 0.016 711 3° and 0.107 815 deg/s, respectively. All the in situ XRD measurements were performed in a helium environment.

2.3. Scanning Electron Microscopy and Energy-Dispersive X-ray Spectroscopy. Surface morphological images were taken with a Zeiss Merlin scanning electron microscope (SEM) operated at 5 kV using the in-lens mode and line average scanning. Energy dispersive X-ray spectroscopy (EDS) was acquired at an accelerating voltage of 20 kV and a tilt angle of 45°, leading to a penetration depth of ∼2 μm.

2.4. Time-of-Flight Secondary Ion Mass Spectrometry. TOF-SIMS data was acquired with a TOF-SIMS 5 (ION-TOF, Münster, Germany) using a 30 keV Bi ion primary gun with a spot size of ∼100 nm. The images were collected with a resolution of 256 × 256 pixels spread across a 20 × 20 μm area. Depth profiling of the sample was carried out using a Cs sputtering source operated at 1 keV and 75 nA and sputtering for 5 s per slice. The data was collected in positive ion mode with Cl and I forming Cs_2Cl^+ and Cs_2I^+ clusters.

2.5. Density Functional Theory Calculations. VASP code[13] was used to perform density functional theory calculations. Both the Perdew−Burke−Ernzerhof (PBE) functional[14] and the nonlocal vdW-TS functional,[15] which incorporates the description of the van der Waals interaction, were used to calculate the energy change for reactions (9) and (10). The ion-electron interaction was described by the projector augmented-wave method.[16] The wave functions were expanded in a plane-wave basis set with a cutoff energy of 500 eV. The atoms were relaxed until the force on each atom was less than 0.01 eV/Å.

3. RESULTS AND DISCUSSION

3.1. Perovskite Crystallization Kinetics. A large variety of synthesis and processing approaches, such as sequential processing,[1a,17] thermal evaporation,[1c,18] and mixed-solution methods,[1b,d,12a] have been developed to grow OHP thin films. Among them, the vapor-assisted method developed by Chen et al.[19] has attracted significant attention due to the high-quality films reproducibly produced with pinhole-free morphology and large grains. This approach has also been proven applicable for the fabrication of optoelectronic devices, such as solar cells. Following procedures as described in the Experimental Section, we fabricated solar cells with a glass/ITO(indium tin oxide)/TiO_2/$CH_3NH_3PbI_3$/Spiro-OMeTAD/Ag architecture. As shown in Figure S1 of the Supporting Information (SI), when measured in the forward scan mode (sweep from +1.2 V to −0.2 V), the typical device yielded a short-circuit current density (J_{SC}) of 19.5 mA/cm^2, an open-circuit voltage (V_{OC}) of 1.004 V, a fill factor (FF) of 67%, and a power conversion efficiency (PCE) of 13.2%, which is comparable to other reports.[19,20] However, when measured in the reverse scan mode (scan from −0.2 V to +1.2 V), this device output inferior photovoltaic parameters, i.e., a J_{SC} of 19.6 mA/cm^2, an V_{OC} of 0.902 V, a FF of 50%, and a PCE of 8.9%. Due to this severe J-V hysteresis, the stabilized power output was further characterized by measuring the photocurrent at a maximum power output point of ∼0.78 V, yielding a stabilized PCE of 8.9%, which is suitable for photovoltaic applications. It should be noted that the device performance was not optimized in our work, since this was not the focus of this study.

In order to understand the crystal nucleation and growth processes in the films grown by the vapor-assisted method, we employed in situ XRD to monitor the structural evolution in the samples. As shown in Figure 1a, spun-cast PbI_2 films on glass substrates were placed on a ceramic sample stage within a special reaction chamber. CH_3NH_3I powder was dispersed around the PbI_2 film, and the sample stage was controllably heated. An inert gas (helium) was purged to avoid sample degradation.[19] At a temperature close to the CH_3NH_3I boiling point, CH_3NH_3I vapor molecules are generated and diffused into the PbI_2 film to initiate the reaction between CH_3NH_3I and PbI_2 for the nucleation and growth of $CH_3NH_3PbI_3$ crystals. Given an ample supply of vapor, the crystallization rate (reaction rate) is mainly controlled by the diffusion rate of the CH_3NH_3I molecules into the compact PbI_2 layer.

DOI: 10.1021/jacs.5b13254
J. Am. Chem. Soc. 2016, 138, 5028−5035

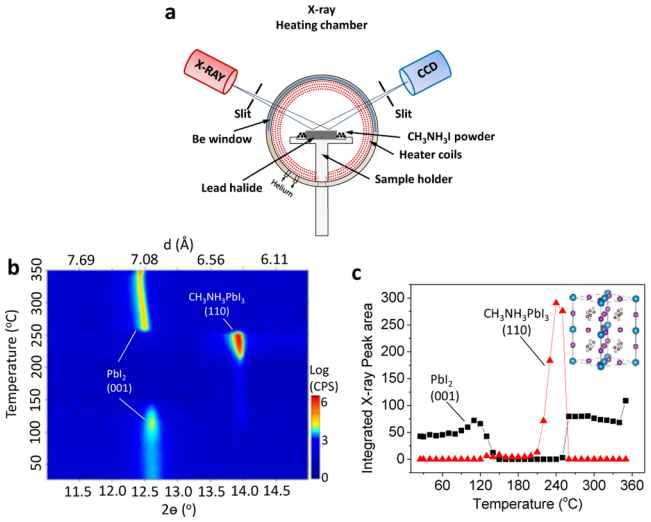

Figure 1. In situ X-ray study of reactive synthesis of $CH_3NH_3PbI_3$ perovskite films. (a) A schematic illustration of the in situ X-ray diffraction (XRD) measurement setup. A spun-cast PbI_2 film on a glass substrate was placed on a ceramic sample stage, and the CH_3NH_3I powder was dispersed around the PbI_2 film followed by controlled heating in a reaction chamber, where the helium gas was circulated to avoid sample degradation. (b) Contour plots for temperature-dependent XRD to monitor the variation of 2θ for (001) of PbI_2 and for (110) of $CH_3NH_3PbI_3$. (c) Variation of integrated peak areal intensity, where the inset shows the crystal structure of $CH_3NH_3PbI_3$ perovskite (blue balls represent Pb, purple balls represent I, brown balls represent C, and gray balls represent N).

The crystallization kinetics were measured by series of X-ray diffractograms recorded during temperature ramp experiments, as shown in Figure 1b. In the figure, the observed diffraction peaks at 2θ = 12.65° and 14.05° represent the (001) reflection of the PbI_2 precursor and the (110) reflection of the crystalline $CH_3NH_3PbI_3$ reaction product, respectively. By fitting the peaks and extracting the peak areas for crystalline $CH_3NH_3PbI_3$ and PbI_2, their relative populations as a function of temperature can be plotted, as shown in Figure 1c. First, it can be seen that the crystallinity in the PbI_2 precursor film increases as the temperature is raised to 110 °C. Increasing the temperature above 110 °C results in an emergence of the (110) reflection of $CH_3NH_3PbI_3$ crystals concurrent with a decrease in the intensity of (001) reflection of PbI_2 crystals, revealing that CH_3NH_3I molecules began to evaporate and diffuse into the PbI_2 layer at a temperature of 120 °C to induce the solid state reaction and crystallization of $CH_3NH_3PbI_3$ perovskite. By 150 °C, the PbI_2(001) reflection disappears completely, implying that PbI_2 has been fully consumed in the reaction with CH_3NH_3I. At 200 °C, the $CH_3NH_3PbI_3$(110) reflection began to increase rapidly, indicating a region of rapid crystal growth, reaching a maximum at 240 °C. We interpret the temperature range between 150 and 200 °C, where the fraction of ordered $CH_3NH_3PbI_3$ is still very low, as the nucleation stage. The enhancement in the $CH_3NH_3PbI_3$(110) reflection in the 200–240 °C temperature range suggests that the initially low fraction of crystalline grains oriented in the [110] direction led to the increase in crystallinity. Further increasing the temperature above 240 °C gave rise to a sharp drop in the $CH_3NH_3PbI_3$(110) reflection intensity together with a reemergence of the PbI_2(001) reflection. The sharp decrease in the $CH_3NH_3PbI_3$(110) reflection area is likely due to the thermal decomposition of $CH_3NH_3PbI_3$ perovskite, which leads to the formation of PbI_2.

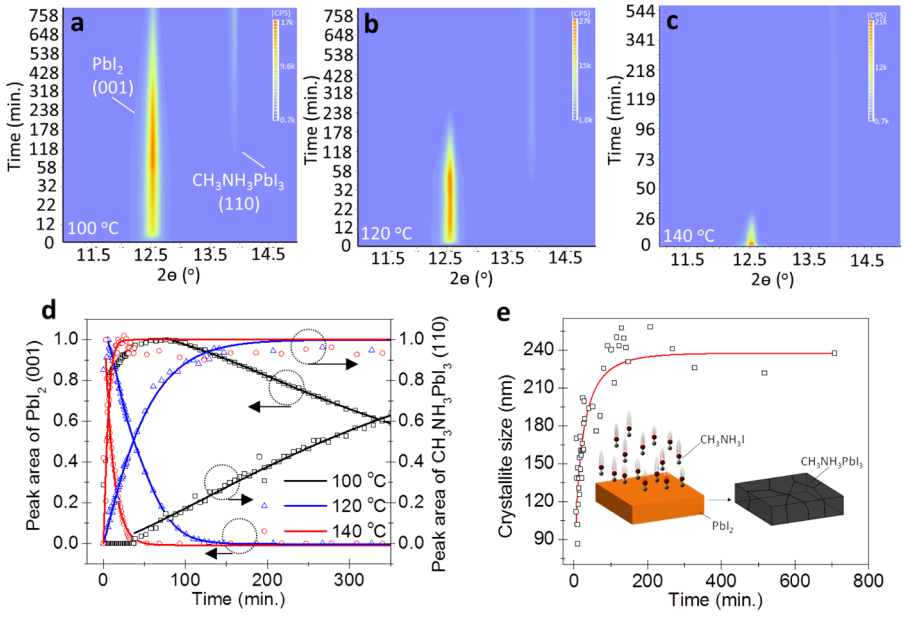

Figure 2. Crystallization kinetics of $CH_3NH_3PbI_3$ perovskites. Time-dependent contour plot of XRD patterns at three growth temperatures, (a) 100 °C, (b) 120 °C, and (c) 140 °C, to reveal the dynamics of the growth of $CH_3NH_3PbI_3$ perovskite crystals via the chemical reaction (PbI_2 + CH_3NH_3I→ $CH_3NH_3PbI_3$). The XRD pattern at t = 0 min was acquired at room temperature. (d) Time-dependent variations of normalized peak area of PbI_2(001) and $CH_3NH_3PbI_3$(110) at three growth temperatures (100 °C, black squares; 120 °C, blue triangles; and 140 °C, red circles). The corresponding solid lines are a result of Avrami model fits. (e) The crystallite size calculated by the Scherrer equation reveals that the crystallite grows along the direction perpendicular to the substrate from top to bottom, known as one-dimensional growth, and then reaches the bottom substrate at ∼130 min. Squares show the calculated crystallite size with time at 120 °C, and the red curve is used to guide the eye. Inset of part e shows a schematic of the reaction between CH_3NH_3I vapor and the PbI_2 film to form perovskites.

DOI: 10.1021/jacs.5b13254
J. Am. Chem. Soc. 2016, 138, 5028–5035

In an effort to investigate the isothermal nucleation and growth processes of $CH_3NH_3PbI_3$ crystals, we chose three growth temperatures, i.e., 100, 120, and 140 °C. Again, time-resolved in situ XRD was applied to monitor the evolution of the $CH_3NH_3PbI_3(110)$ and $PbI_2(001)$ reflections. The contour plots for the time-dependent X-ray diffraction patterns at 100, 120, and 140 °C are shown in parts a, b, and c of Figure 2, respectively. Correspondingly, Figure 2d depicts the time-dependent variations in the integrated peak area of $PbI_2(001)$ and $CH_3NH_3PbI_3(110)$ during the reaction at each temperature. As shown in Figure 2a–c, the onset time of crystallization identified by the emergence of $CH_3NH_3PbI_3(110)$ reflection is strongly temperature-dependent. It should be noted that the film grown at 100 °C for ~920 min contained a large portion of unreacted PbI_2, as suggested by the existence of the $PbI_2(001)$ reflection at 12.65° (Figure 2a) and the corresponding surface morphology in SEM image (Figure S2, SI), most likely resulting from the low diffusivity of CH_3NH_3I molecules combined with the low CH_3NH_3I vapor pressure at 100 °C. The perovskite crystallization kinetics at different growth temperatures was modeled using the generalized Avrami approach,[21] which describes materials transforming from one phase to another with time under isothermal condition (eqs 1 and 2)

$$v(t) = 1 - \exp(-kt^n) \quad (1)$$

$$\ln[-\ln(1 - v(t))] = \ln k + n \ln t \quad (2)$$

where $v(t)$ is the fraction (I_t/I_{final}) of peak area at time = t (I_t) over the final peak area at $t = \infty$ and k is the crystal growth rate constant. The Avrami exponent (n) is obtained from the slope of the initial linear parts of the curves depicted in Figure S3 (SI). The Avrami model suggests the balance between the rates for nucleation and crystal growth, as well as the crystal transformation geometry and growth mechanism.[22] The values of the Avrami exponent (n) and crystal growth rate (k) obtained from the generalized Avrami model fit for different growth temperatures are presented in Table S1 (SI). It is observed that k increases significantly with increasing temperature, and this is not surprising, because the molecular diffusion to the growth front of crystals is strongly temperature-dependent. The plot of k versus the isothermal crystallization temperature, fitted with the Arrhenius equation (Figure S3, SI), allowed an activation energy for $CH_3NH_3PbI_3$ crystal growth of 182.8 kJ/mol to be estimated. In principle, a value of n from 0.5 to 1.5 indicates a diffusion-controlled reaction and one-dimensional growth, where an $n \sim 0.5$ indicates instantaneous nucleation and $n \sim 1.5$ signifies nucleation with a constant nucleation rate with respect crystallization time.[23] As shown in Table S1 (SI), it can be seen that n falls into the range from 1 to 1.5, indicating that the crystals formed here result from diffusion-controlled, one-dimensional growth involving constant nucleation.[23] Figure 2e shows the crystallite size calculated from the Scherrer equation vs growth time at the temperature of 120 °C. The crystallite size of the perovskite at 130 min (when PbI_2 becomes completely consumed) is similar to the thin film thickness, suggesting that the one-dimensional growth behavior ends with the top-down reaction of the film, as illustrated in the inset of Figure 2e. The combined data indicate that the CH_3NH_3I vapor initially reacts with the PbI_2 on the upper surface to form a thin layer of perovskite crystal nuclei followed by diffusion of CH_3NH_3I molecules through this layer (likely at evolving grain boundaries) to react with PbI_2 below, promoting $CH_3NH_3PbI_3$ crystal growth along the direction perpendicular to the substrate from top to bottom. Following this one-dimensional nucleation and growth, the XRD data suggest that the $CH_3NH_3PbI_3$ grains coalesce laterally to form large grains.

3.2. Examining the Competition between I^- and Br^- by in Situ X-ray Study. Inspired by this understanding of the nucleation and growth mechanisms for $CH_3NH_3PbI_3$ pure triiodide perovskite crystals, we performed additional investigations of CH_3NH_3I interactions with mixed lead halide (PbI_2 and $PbBr_2$) precursor films to address the competition between iodine (I^-) and bromine (Br^-) ions during perovskite synthesis. To understand this reaction, we tracked the characteristic Bragg peaks at 11.24° for $PbBr_{1.2}I_{0.8}$·DMF(003), 13.18° for orthorhombic phase $PbBr_{1.2}I_{0.8}(110)$, 12.64° for $PbI_2(001)$, 13.95° for $CH_3NH_3PbI_3(110)$, and 14.59° for $CH_3NH_3PbI_{1.5}Br_{1.5}(110)$. A two-dimensional (2D) graph of time-dependent X-ray diffraction patterns measured at 120 °C during the reaction is shown in Figure 3a. It should be noted

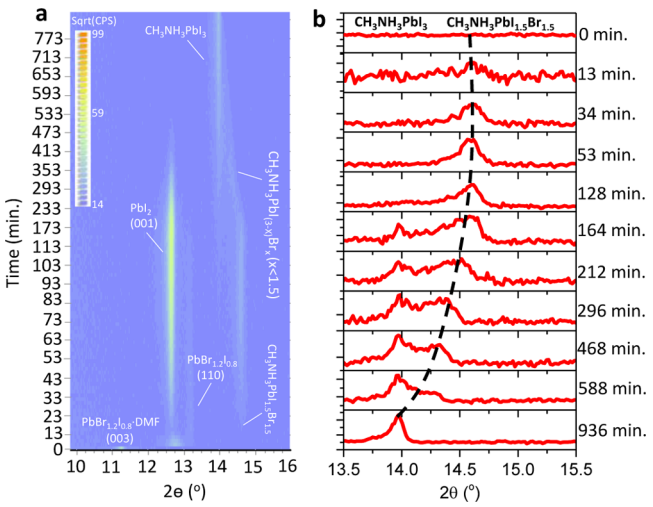

Figure 3. Competition between I^- and Br^- during synthesis of perovskites. (a) Time-dependent contour plots for isothermal XRD patterns measured at 120 °C to monitor the variation of Bragg peaks at 11.24° for $PbBr_{1.2}I_{0.8}$·DMF(003), 13.18° for $PbBr_{1.2}I_{0.8}(110)$, 12.64° for $PbI_2(001)$, 13.95° for $CH_3NH_3PbI_3(110)$, and 14.59° for $CH_3NH_3PbI_{1.5}Br_{1.5}(110)$. The XRD pattern for t = 0 min was acquired at room temperature. (b) The continuous Bragg peak shift from 14.59° to 13.95° suggesting a dynamic phase transformation from $CH_3NH_3PbI_{1.5}Br_{1.5}$ to $CH_3NH_3PbI_3$ with increasing reaction time.

that the as-cast precursor film, obtained from spin-coating a mixed solution of PbI_2 and $PbBr_2$ in DMF solvent, is composed of a $PbBr_{1.2}I_{0.8}$·DMF composite (Figure S4, SI), where the DMF is intercalated between $PbBr_{1.2}I_{0.8}$ 2D layers through the Pb–O coordination bond to bridge $PbBr_{1.2}I_{0.8}$ and DMF molecules.[24] As indicated by XRD, the $PbBr_{1.2}I_{0.8}$·DMF composite completely decomposed by releasing DMF when annealed at 100 °C for 1 min (Figure S4, SI) and is consistent with thermogravimetric analysis reported by Wakamiya et al.[24] Thus, as shown in Figure 3a, the XRD pattern acquired at room temperature (t = 0 min) indicates the presence of $PbBr_{1.2}I_{0.8}$·DMF, as evidenced by the (003) peak at 11.24°. This peak immediately disappeared when the reaction temperature was increased to 120 °C and was accompanied by the simultaneous appearance of the peak at 13.18°, which corresponded to $PbBr_{1.2}I_{0.8}(110)$ crystals. This revealed that the initial

DOI: 10.1021/jacs.5b13254
J. Am. Chem. Soc. 2016, 138, 5028–5035

$PbBr_{1.2}I_{0.8}$·DMF composite decomposed to a thermodynamically stable $PbBr_{1.2}I_{0.8}$ phase (Figure S4, SI). Further annealing at 120 °C resulted in the diffusion of CH_3NH_3I vapor molecules into the $PbBr_{1.2}I_{0.8}$ film to form two products, PbI_2 and $CH_3NH_3PbI_{1.5}Br_{1.5}$, as suggested by the emergence of peaks centered at 12.64° for PbI_2 and 14.59° for $CH_3NH_3PbI_{1.5}Br_{1.5}$,[25] respectively (Figure 3a). The evolution of the $PbBr_{1.2}I_{0.8}$ and PbI_2 XRD peaks in the CH_3NH_3I vapor environment was plotted in Figure S5 (SI), and it was observed that the peak area of PbI_2(001) at 12.64° progressively increased, reaching a maximum at 128 min, whereas the peak area of $PbBr_{1.2}I_{0.8}$(001) at 13.18° simultaneously decreased and disappeared at 128 min. These observations indicated that Br^- from $PbBr_{1.2}I_{0.8}$ was gradually substituted with I^- from CH_3NH_3I, most likely due to more reactive nature of I^- than Br^-.[25,26] Similarly, a dynamic phase transformation from $CH_3NH_3PbI_{1.5}Br_{1.5}$ to $CH_3NH_3PbI_3$ was observed (Figure 3b), as evidenced by the continuous Bragg peak shift from 14.59° to 13.95°. As suggested by the gradual disappearance of the PbI_2(001) peak and simultaneous increase in the $CH_3NH_3PbI_3$(110) peak, another phase evolution that occurred at this stage was the formation of $CH_3NH_3PbI_3$ that resulted from the consumption of PbI_2. In addition, we have performed an experiment to examine what happens when using a methylammonium bromide (CH_3NH_3Br) and CH_3NH_3I powder mixture to generate a methylammonium mixed-halide vapor and a pure PbI_2 thin film as a precursor. The time-dependent contour plots for isothermal XRD patterns measured at 120 °C are shown in Figure S6 (SI). Interestingly, the mixed-halide perovskite $CH_3NH_3PbI_{3-x}Br_x$ was not observed by in situ XRD measurements. This result is distinguished from that obtained when using mixed lead halide PbI_2 and $PbBr_2$ (in the form of a thermodynamically stable phase $PbBr_{1.2}I_{0.8}$) precursor films to react with CH_3NH_3I vapor, as shown in Figure 3. On the basis of our understanding, such a discrepancy is not surprising. For the former, the CH_3NH_3I molecules would intercalate into the $PbBr_{1.2}I_{0.8}$ 2D layers to form mixed-halide perovskite crystal $CH_3NH_3PbI_{3-x}Br_x$. For the latter, however, only the CH_3NH_3I molecules can intercalate into the well-oriented PbI_2 2D layers to form pure iodide perovskite crystal $CH_3NH_3PbI_3$,[27] because in the presence of excessive CH_3NH_3I, the CH_3NH_3Br would not participate in the chemical reaction. In other words, in the presence of excessive reactive I^- ions, Br^- ions are not incorporated into the final perovskite crystal structure.

To examine where the Br^- ultimately resided in the films, we performed EDS characterization along with SEM imaging. The SEM image showed that micrometer-size flakes were present on the perovskite film surface, which primarily contain Br, I, and N, as suggested by EDS mapping (Figure S7, SI). To identify the composition of the flake, an EDS spectrum was acquired, and it showed that the atomic ratio of Br, I, N, and Pb was about 1.15:0.95:1:0.18 (Figure S7, SI). Since the penetration depth of the electron beam was ~2 μm for an accelerating voltage of 20 kV, the poor Pb signal most likely originated from underneath the $CH_3NH_3PbI_3$ perovskite layer, as evidenced by the strong X-ray signal collected from other elements, such as indium and silicon from the ITO glass substrate. Consequently, the flakes were most likely $CH_3NH_3I_{1-x}Br_x$, and it should be noted that the quantitative identification of the chemical formula of $CH_3NH_3I_{1-x}Br_x$ is challenging from the EDS measurements due to the deep penetration of ~2 μm, which is far beyond the thickness of the flake of around 100 nm. In summary, the formation process of $CH_3NH_3PbI_3$ induced by in situ chemical reactions of the mixed (I, Br) lead halide precursor can be described in the system of reactions 3–5:

$$\text{stage 1:}\quad PbBr_{1.2}I_{0.8}\cdot DMF \rightarrow PbBr_{1.2}I_{0.8} + DMF\uparrow \tag{3}$$

$$\text{stage 2:}\quad CH_3NH_3I + PbBr_{1.2}I_{0.8} \rightarrow PbI_2 + CH_3NH_3I_{1-x}Br_x + CH_3NH_3PbI_{1.5}Br_{1.5} \tag{4}$$

$$\text{stage 3:}\quad CH_3NH_3PbI_{1.5}Br_{1.5} + PbI_2 + CH_3NH_3I \rightarrow CH_3NH_3PbI_3 + CH_3NH_3I_{1-x}Br_x \tag{5}$$

3.3. Examining the Competition between I^- and Cl^- by in Situ X-ray Study. Similarly, in situ X-ray diffraction was applied to monitor phase evolution in the mixed lead halide (PbI_2, $PbCl_2$) system to reveal the competition between I^- and Cl^- ions during perovskite synthesis. First, it is worth mentioning that the PbI_2 and $PbCl_2$ in the DMSO solvent reacted with each other to form a Pb(Cl)I compound (Figure S8, SI), and as such, the initial state of the precursor film at room temperature (0 min in Figure 4) was composed of Pb(Cl)I, rather than PbI_2 and $PbCl_2$. As before, CH_3NH_3I vapor molecules were driven to diffuse into the Pb(Cl)I layer at 120 °C, and as shown in Figure 4, over time the PbI_2(001) peak at 12.64° and $CH_3NH_3PbI_3$(110) peak at 13.95° appeared simultaneously while the Pb(Cl)I(011) peak at 21.26° diminished. After 40 min, the intensity of the PbI_2(001) peak started decreasing while the $CH_3NH_3PbI_3$(110) peak increased, indicating that the PbI_2 created from the Pb(Cl)I compound was finally consumed by the CH_3NH_3I vapor to form $CH_3NH_3PbI_3$. Since the Bragg peaks for $PbCl_2$ (e.g., 22.06°, 29.86°, and 39.04°) were not detected, it is speculated that the Cl^- may be present in amorphous $PbCl_2$ (ref 11b) or perhaps some other amorphous phase.[10c] Furthermore, the absence of Bragg peaks for $CH_3NH_3PbCl_3$ (e.g., 15.50°) and mixed-(I, Cl) perovskites (indicated by peaks between 14.05° and 15.50°) during the entire reaction process suggests that neither $CH_3NH_3PbCl_3$ nor mixed (I, Cl) perovskite was formed. Given these observations, it is most likely that the Cl^- was not

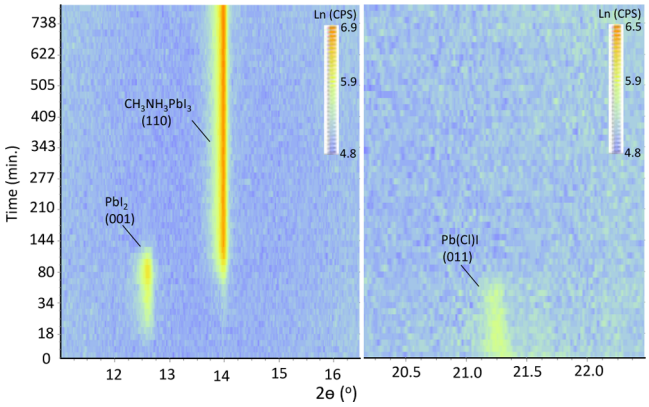

Figure 4. Competition between I^- and Cl^- during synthesis of perovskites. Time-dependent contour plots for the isothermal XRD patterns acquired at 120 °C to monitor the variation of Bragg peaks at 12.64° for PbI_2(001), 13.95° for $CH_3NH_3PbI_3$(110), and 21.26° for Pb(Cl)I(011).

DOI: 10.1021/jacs.5b13254
J. Am. Chem. Soc. 2016, 138, 5028–5035

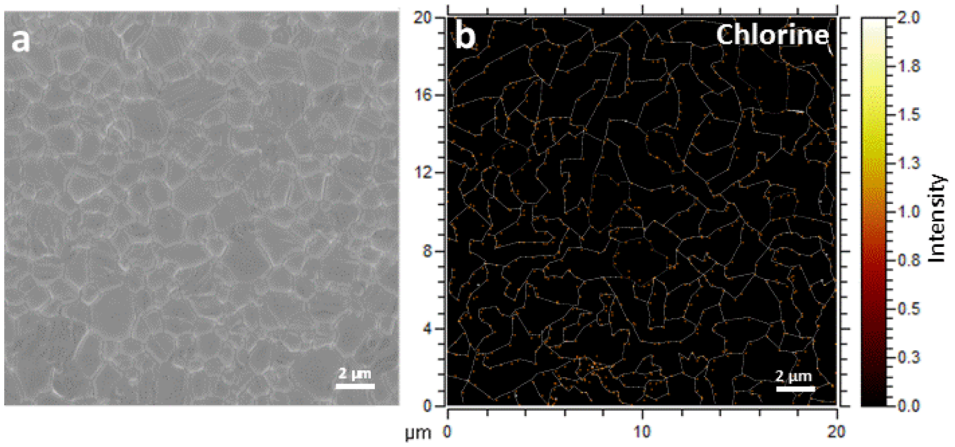

Figure 5. TOF-SIMS elemental mapping and analysis. The $CH_3NH_3PbI_3$ perovskite film was obtained using a (I, Cl)-based lead halide as a precursor for an in situ reaction. (a) A typical SEM image acquired from the $CH_3NH_3PbI_3$ perovskite film and (b) Cl mapping image suggesting that Cl^- sits in the grain boundaries, where the yellow dots indicate the location of Cl^- and the dotted line (guiding eyes) network indicates grains with sizes comparable to those observed in the SEM image (panel a).

incorporated into the perovskite crystal structure in the presence of more chemically reactive I^-.[26b]

To understand where the Cl^- resides in these films, time-of-flight secondary ion mass spectrometry (TOF-SIMS) was used because of its high sensitivity capability. During our measurements, a focused cesium ion beam was used for sputtering the perovskite film to allow for depth profiling, and a focused bismuth ion beam was used as the primary analysis beam to generate secondary ions for elemental mapping. A set of images that display the summed elemental signals (Pb, I, and Cl) obtained from a sample with a dimension of 350 nm × 20 μm × 20 μm ($Z \times X \times Y$) are shown in Figure S9 (SI). It was found that the Cl is present in the film, but with a concentration far less than that of Pb or I. These observations reveal unambiguously that the Cl^- remains in the $CH_3NH_3PbI_3$ perovskite film despite the absence of XRD peaks associated with Cl^--based perovskites or other compounds (Figure 4). As mentioned by Snaith and co-workers, a slight amount of Cl compared to either I or Pb is likely the result of evaporation of the reaction product, CH_3NH_3Cl, during annealing.[28] To further understand the Cl^- distribution, we acquired a SEM image of the perovskite film to characterize its surface morphology, which was found to exhibit an average grain size of ~1 μm (Figure 5a). It should be noted that although the TOF-SIMS instrument had imaging capabilities, it was not suitable for high-resolution imaging due to the size of its primary beam (~100 nm); i.e., it was hard to distinguish small grains (~1 μm) and grain boundaries (Figure S10, SI), hence the use of a separate SEM image. To avoid surface artifacts, we sputtered the sample to remove surface carbon, etc., and then examined the subsurface Cl^- distribution. Interestingly, it was found that the distribution of Cl^- (yellow dots) formed a network (Figure 5b) that resembled the distribution of grains found in the SEM image (Figure 5a) and with similar dimensions (20 × 20 μm). These observations strongly suggest that the Cl^- sits in the grain boundaries, rather than in the perovskite crystal lattice.

On the basis of the time-resolved in situ XRD analysis, the chemical reaction process that involves mixed (I, Cl) lead halide may be described by the following reactions 6–8:

$$\text{stage 1:}\quad PbI_2 + PbCl_2 \rightarrow Pb(Cl)I \tag{6}$$

stage 2:

$$Pb(Cl)I + CH_3NH_3I \rightarrow PbI_2 + CH_3NH_3PbI_3 + PbCl_2 \tag{7}$$

$$\text{stage 3:}\quad PbI_2 + CH_3NH_3I \rightarrow CH_3NH_3PbI_3 \tag{8}$$

3.4. Density Functional Theory Calculations. Although a dynamic phase transformation from $CH_3NH_3PbI_{1.5}Br_{1.5}$ to $CH_3NH_3PbI_3$ was observed when mixed (I, Br) lead halide was employed as a precursor in the presence of CH_3NH_3I vapor, we did not observe a similar phenomenon when mixed (I, Cl) lead halide was used. Furthermore, a mixed (I, Cl) perovskite was not observed during the entire reaction process in the latter case, and these results suggest that Cl^- and Br^- affect perovskite crystal formation differently. To further understand the origin of this difference, we evaluated the reaction energy for transformation reactions 9 and 10 between Br^-- or Cl^-- and I^--based perovskites in the presence of CH_3NH_3I vapor using density functional theory (DFT) calculations.

$$CH_3NH_3PbBr_3 + 3CH_3NH_3I \rightarrow CH_3NH_3PbI_3 + 3CH_3NH_3Br \tag{9}$$

$$CH_3NH_3PbCl_3 + 3CH_3NH_3I \rightarrow CH_3NH_3PbI_3 + 3CH_3NH_3Cl \tag{10}$$

DFT calculations using PBE and vdW-TS functionals show that reaction 9 lowers the energy by −0.07 and −0.25 eV, respectively, indicating that the ion-exchange reaction (transforming $CH_3NH_3PbBr_3$ to $CH_3NH_3PbI_3$) is exothermic. The reaction for transforming $CH_3NH_3PbI_{1.5}Br_{1.5}$ to $CH_3NH_3PbI_3$ should be energetically more favorable because mixing size-mismatched halogens in $CH_3NH_3PbI_{1.5}Br_{1.5}$ incurs higher strain energy, and consequently, the formation of pure $CH_3NH_3PbI_3$ by ion exchange releases more energy.[29] We also calculated the energy change for reaction 10, which was found to be −0.22 and −0.31 eV by using PBE and vdW-TS functionals, respectively. The reaction involving Cl^- (reaction 10) is significantly more exothermic than the chemical reaction involving Br^- (reaction 9), indicating that forming $CH_3NH_3PbCl_3$, $CH_3NH_3PbI_{1.5}Cl_{1.5}$, or other mixed (I, Cl) perovskites in the presence of CH_3NH_3I vapor is much more

DOI: 10.1021/jacs.5b13254
J. Am. Chem. Soc. 2016, 138, 5028–5035

difficult than forming their bromide counterparts. This may explain the absence of mixed (I, Cl) perovskites during the growth observed in our in situ X-ray experiments. These results are also consistent with recently reported first-principles calculations that show that the mixed (I, Cl) perovskite is structurally hard to form at high temperatures (e.g., 120 °C in our experiment) due to a large formation energy resulting from differences in ion sizes; i.e., I^- = 2.07 Å, whereas Cl^- = 1.67 Å.[29] In contrast, the formation of mixed (I, Br) perovskites costs much less energy due to a small difference in ion size (I^- = 2.07 Å is closer in size to Br^- = 1.84 Å).[29]

To further elucidate the role of halogens (e.g., Br and Cl) during the synthesis and growth of $CH_3NH_3PbI_3$ perovskites, we applied SEM imaging to examine the perovskite grain size and surface morphology in three individual $CH_3NH_3PbI_3$ perovskite films that were obtained from pure PbI_2, (I, Br) mixed halide, and (I, Cl) mixed halide, after their chemical reactions with CH_3NH_3I for identical times and temperatures (~810 min and 120 °C, respectively). As shown in Figure 6, the

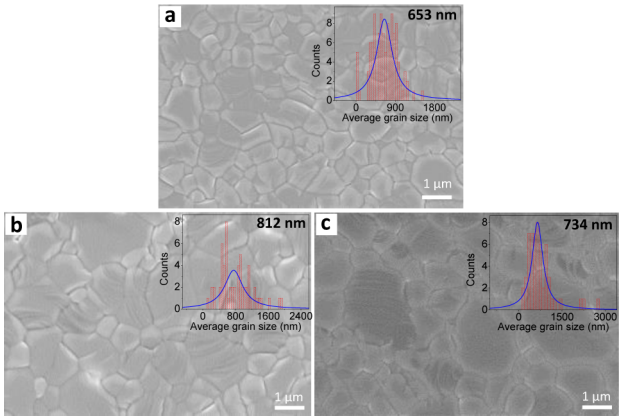

Figure 6. Comparison of grain size. SEM images of the surface morphologies of the perovskite films obtained after in situ reaction for ~810 min at 120 °C using different precursors, (a) pure PbI_2, (b) (I, Br) mixed halide, and (c) (I, Cl) mixed halide, showing average grain size of ~653 nm (a), ~ 812 nm (b), and ~734 nm (c), respectively. Inset figures display the distribution of grain sizes. The blue line is fitted by the Lorenz function.

perovskite films, obtained from a (I, Br) mixed halide and a (I, Cl) mixed halide, exhibit an average grain size of ~812 nm (Figure 6b) and ~734 nm (Figure 6c), respectively, which appear larger than the average grain size (~653 nm) obtained from pure PbI_2 (Figure 6a), indicating that both Br and Cl may promote crystal growth in $CH_3NH_3PbI_3$ perovskite films. This result is reasonably consistent with recent reports that showed that the presence of Cl during the reaction of PbI_2 and CH_3NH_3I can significantly promote the crystallization of $CH_3NH_3PbI_3$[10c] and thereby enhance carrier transport properties and increase the photovoltaic performance in solar cells.[7c,11c,i]

4. CONCLUSIONS

The crystallization kinetics of the perovskite $CH_3NH_3PbI_3$ was characterized by in situ XRD and found to exhibit a diffusion-controlled, one-dimensional growth mechanism in accordance with the Avrami model. The results indicate that during the crystallization process, crystal nuclei form at a constant rate and grow in a direction perpendicular to the substrate surface. During this crystal growth stage the growth rate is governed by the diffusion rate of the CH_3NH_3I precursor to the crystal growth front. After this one-dimensional growth process, the data indicate that the crystals continue to evolve to form large grains by coalescence. The competition between halides when employing mixed-halide starting materials was also elucidated. For both mixed (I, Br) or mixed (I, Cl) lead halide starting material, remarkably both reactions in a CH_3NH_3I vapor environment led to the formation of $CH_3NH_3PbI_3$, revealing that in the presence of reactive I^- ions neither Br^- nor Cl^- is incorporated into the final perovskite crystal structure. However, both Br^- and Cl^- ions promote grain growth, enhancing the carrier transport properties in $CH_3NH_3PbI_3$ perovskite films. Importantly, chemical imaging and mapping with TOF-SIMS reveals that the Cl^- resides in the grain boundaries of these films, possibly in the form of an amorphous Cl^--based compound. This combination of in situ studies, chemical imaging, and modeling has advanced our understanding of the role of halogens during synthesis of hybrid perovskites and provides insight and guidance to aid in developing a controllable process to synthesize and grow high-quality perovskite films for high-performance optoelectronic devices.

■ ASSOCIATED CONTENT

Supporting Information

These materials are available free of charge via the Internet at The Supporting Information is available free of charge on the ACS Publications website at DOI: 10.1021/jacs.5b13254.

Device performance, SEM image of the $CH_3NH_3PbI_3$ perovskite film in situ grown at 100 °C, Avrami model fit, XRD patterns of the as-casted film, and SEM/EDS and TOF-SIMS of $CH_3NH_3PbI_3$ film (Figures S1−S10 and Table S1) (PDF)

■ AUTHOR INFORMATION

Corresponding Author

*xiaok@ornl.gov

Notes

The authors declare no competing financial interests.

■ ACKNOWLEDGMENTS

This research was conducted at the Center for Nanophase Materials Sciences (CNMS), which is a DOE Office of Science User Facility. M.H.D.'s work is supported by the Department of Energy, Office of Science, Basic Energy Sciences, Materials Sciences and Engineering Division. The authors acknowledge Ho Ming Tong for preparation of contour plots (Figure 1b).

■ REFERENCES

(1) (a) Burschka, J.; Pellet, N.; Moon, S.-J.; Humphry-Baker, R.; Gao, P.; Nazeeruddin, M. K.; Grätzel, M. *Nature* **2013**, *499*, 316−319. (b) Jeon, N. J.; Noh, J. H.; Yang, W. S.; Kim, Y. C.; Ryu, S.; Seo, J.; Seok, S. I. *Nature* **2015**, *517*, 476−480. (c) Liu, M.; Johnston, M. B.; Snaith, H. J. *Nature* **2013**, *501*, 395−398. (d) Yang, W. S.; Noh, J. H.; Jeon, N. J.; Kim, Y. C.; Ryu, S.; Seo, J.; Seok, S. I. *Science* **2015**, *348*, 1234−1237.

(2) (a) Kim, Y. H.; Cho, H.; Heo, J. H.; Kim, T. S.; Myoung, N.; Lee, C. L.; Im, S. H.; Lee, T. W. *Adv. Mater.* **2015**, *27*, 1248−1254. (b) Tan, Z.-K.; Moghaddam, R. S.; Lai, M. L.; Docampo, P.; Higler, R.; Deschler, F.; Price, M.; Sadhanala, A.; Pazos, L. M.; Credgington, D.; et al. *Nat. Nanotechnol.* **2014**, *9*, 687−692.

DOI: 10.1021/jacs.5b13254
J. Am. Chem. Soc. 2016, 138, 5028−5035

(3) Yakunin, S.; Sytnyk, M.; Kriegner, D.; Shrestha, S.; Richter, M.; Matt, G. J.; Azimi, H.; Brabec, C. J.; Stangl, J.; Kovalenko, M. V.; et al. *Nat. Photonics* **2015**, *9*, 444−449.
(4) (a) Dou, L.; Yang, Y. M.; You, J.; Hong, Z.; Chang, W.-H.; Li, G.; Yang, Y. *Nat. Commun.* **2014**, *5*, 5404. (b) Fang, Y.; Dong, Q.; Shao, Y.; Yuan, Y.; Huang, J. *Nat. Photonics* **2015**, *9*, 679−686.
(5) Kojima, A.; Teshima, K.; Shirai, Y.; Miyasaka, T. *J. Am. Chem. Soc.* **2009**, *131*, 6050−6051.
(6) Eperon, G. E.; Stranks, S. D.; Menelaou, C.; Johnston, M. B.; Herz, L. M.; Snaith, H. J. *Energy Environ. Sci.* **2014**, *7*, 982−988.
(7) (a) Dong, Q.; Fang, Y.; Shao, Y.; Mulligan, P.; Qiu, J.; Cao, L.; Huang, J. *Science* **2015**, *347*, 967−970. (b) Shi, D.; Adinolfi, V.; Comin, R.; Yuan, M.; Alarousu, E.; Buin, A.; Chen, Y.; Hoogland, S.; Rothenberger, A.; Katsiev, K.; et al. *Science* **2015**, *347*, 519−522. (c) Stranks, S. D.; Eperon, G. E.; Grancini, G.; Menelaou, C.; Alcocer, M. J.; Leijtens, T.; Herz, L. M.; Petrozza, A.; Snaith, H. J. *Science* **2013**, *342*, 341−344.
(8) Buin, A.; Comin, R.; Xu, J.; Ip, A. H.; Sargent, E. H. *Chem. Mater.* **2015**, *27*, 4405−4412.
(9) Hao, F.; Stoumpos, C. C.; Chang, R. P.; Kanatzidis, M. G. *J. Am. Chem. Soc.* **2014**, *136*, 8094−8099.
(10) (a) Grancini, G.; Marras, S.; Prato, M.; Giannini, C.; Quarti, C.; De Angelis, F.; De Bastiani, M.; Eperon, G. E.; Snaith, H. J.; Manna, L.; et al. *J. Phys. Chem. Lett.* **2014**, *5*, 3836−3842. (b) Pool, V. L.; Gold-Parker, A.; McGehee, M. D.; Toney, M. F. *Chem. Mater.* **2015**, *27*, 7240−7243. (c) Dar, M. I.; Arora, N.; Gao, P.; Ahmad, S.; Grätzel, M.; Nazeeruddin, M. K. *Nano Lett.* **2014**, *14*, 6991−6996. (d) Unger, E. L.; Bowring, A. R.; Tassone, C. J.; Pool, V. L.; Gold-Parker, A.; Cheacharoen, R.; Stone, K. H.; Hoke, E. T.; Toney, M. F.; McGehee, M. D. *Chem. Mater.* **2014**, *26*, 7158−7165.
(11) (a) Lee, M. M.; Teuscher, J.; Miyasaka, T.; Murakami, T. N.; Snaith, H. J. *Science* **2012**, *338*, 643−647. (b) Gratzel, M. *Nat. Mater.* **2014**, *13*, 838−842. (c) de Quilettes, D. W.; Vorpahl, S. M.; Stranks, S. D.; Nagaoka, H.; Eperon, G. E.; Ziffer, M. E.; Snaith, H. J.; Ginger, D. S. *Science* **2015**, *348*, 683−686. (d) Chae, J.; Dong, Q.; Huang, J.; Centrone, A. *Nano Lett.* **2015**, *15*, 8114−8121. (e) Chen, Q.; Zhou, H.; Fang, Y.; Stieg, A. Z.; Song, T.-B.; Wang, H.-H.; Xu, X.; Liu, Y.; Lu, S.; You, J.; et al. *Nat. Commun.* **2015**, *6*, 7269. (f) Qing, J.; Chandran, H.-T.; Cheng, Y.-H.; Liu, X.-K.; Li, H.-W.; Tsang, S.-W.; Lo, M.-F.; Lee, C.-S. *ACS Appl. Mater. Interfaces* **2015**, *7*, 23110−23116. (g) Williams, S. T.; Zuo, F.; Chueh, C.-C.; Liao, C.-Y.; Liang, P.-W.; Jen, A. K.-Y. *ACS Nano* **2014**, *8*, 10640−10654. (h) Yu, H.; Wang, F.; Xie, F.; Li, W.; Chen, J.; Zhao, N. *Adv. Funct. Mater.* **2014**, *24*, 7102−7108. (i) Colella, S.; Mosconi, E.; Fedeli, P.; Listorti, A.; Gazza, F.; Orlandi, F.; Ferro, P.; Besagni, T.; Rizzo, A.; Calestani, G.; et al. *Chem. Mater.* **2013**, *25*, 4613−4618.
(12) (a) Nie, W.; Tsai, H.; Asadpour, R.; Blancon, J.-C.; Neukirch, A. J.; Gupta, G.; Crochet, J. J.; Chhowalla, M.; Tretiak, S.; Alam, M. A.; Wang, H.-L.; Mohite, A. D. *Science* **2015**, *347*, 522−525. (b) Rong, Y.; Tang, Z.; Zhao, Y.; Zhong, X.; Venkatesan, S.; Graham, H.; Patton, M.; Jing, Y.; Guloy, A. M.; Yao, Y. *Nanoscale* **2015**, *7*, 10595−10599. (c) Yang, B.; Dyck, O.; Poplawsky, J.; Keum, J.; Puretzky, A.; Das, S.; Ivanov, I.; Rouleau, C.; Duscher, G.; Geohegan, D.; et al. *J. Am. Chem. Soc.* **2015**, *137*, 9210−9213.
(13) Kresse, G.; Hafner, J. *Phys. Rev. B* **1994**, *49*, 14251.
(14) Perdew, J. P.; Burke, K.; Ernzerhof, M. *Phys. Rev. Lett.* **1996**, *77*, 3865.
(15) Bučko, T.; Lebègue, S.; Hafner, J.; Ángyán, J. *Phys. Rev. B* **2013**, *87*, 064110.
(16) Blöchl, P. E. *Phys. Rev. B* **1994**, *50*, 17953.
(17) (a) Liu, D.; Kelly, T. L. *Nat. Photonics* **2014**, *8*, 133−138. (b) Yang, B.; Dyck, O.; Poplawsky, J.; Keum, J.; Das, S.; Puretzky, A.; Aytug, T.; Joshi, P. C.; Rouleau, C. M.; Duscher, G.; et al. *Angew. Chem. Int. Ed.* **2015**, *54*, 14862−14865.
(18) Chen, Y.; Chen, T.; Dai, L. *Adv. Mater.* **2015**, *27*, 1053−1059.
(19) Chen, Q.; Zhou, H.; Hong, Z.; Luo, S.; Duan, H.-S.; Wang, H.-H.; Liu, Y.; Li, G.; Yang, Y. *J. Am. Chem. Soc.* **2014**, *136*, 622−625.
(20) (a) Li, Y.; Cooper, J. K.; Buonsanti, R.; Giannini, C.; Liu, Y.; Toma, F. M.; Sharp, I. D. *J. Phys. Chem. Lett.* **2015**, *6*, 493−499. (b) Xia, X.; Li, H.; Wu, W.; Li, Y.; Fei, D.; Gao, C.; Liu, X. *ACS Appl. Mater. Interfaces* **2015**, *7*, 16907−16912.
(21) Avrami, M. *J. Chem. Phys.* **1941**, *9*, 177−184.
(22) (a) Zhou, Y.; Pienack, N.; Bensch, W.; Patzke, G. R. *Small* **2009**, *5*, 1978−1983. (b) Choi, S. Y.; Mamak, M.; Speakman, S.; Chopra, N.; Ozin, G. A. *Small* **2005**, *1*, 226−232.
(23) (a) Kim, W. K.; Payzant, E. A.; Yoon, S.; Anderson, T. J. *J. Cryst. Growth* **2006**, *294*, 231−235. (b) Xiao, K.; Yoon, M.; Rondinone, A. J.; Payzant, E. A.; Geohegan, D. B. *J. Am. Chem. Soc.* **2012**, *134*, 14353−14361.
(24) Wakamiya, A.; Endo, M.; Sasamori, T.; Tokitoh, N.; Ogomi, Y.; Hayase, S.; Murata, Y. *Chem. Lett.* **2014**, *43*, 711−713.
(25) Jang, D. M.; Park, K.; Kim, D. H.; Park, J.; Shojaei, F.; Kang, H. S.; Ahn, J.-P.; Lee, J. W.; Song, J. K. *Nano Lett.* **2015**, *15*, 5191−5199.
(26) (a) Aharon, S.; Cohen, B. E.; Etgar, L. *J. Phys. Chem. C* **2014**, *118*, 17160−17165. (b) Wang, B.; Wong, K. Y.; Xiao, X.; Chen, T. *Sci. Rep.* **2015**, *5*, 10557.
(27) Cheng, H.-C.; Wang, G.; Li, D.; He, Q.; Yin, A.; Liu, Y.; Wu, H.; Ding, M.; Huang, Y.; Duan, X. *Nano Lett.* **2016**, *16*, 367−373.
(28) Zhang, W.; Saliba, M.; Moore, D. T.; Pathak, S. K.; Hörantner, M. T.; Stergiopoulos, T.; Stranks, S. D.; Eperon, G. E.; Alexander-Webber, J. A.; Abate, A.; Sadhanala, A.; Yao, S.; Chen, Y.; Friend, R. H.; Estroff, L. A.; Wiesner, U.; Snaith, H. J. *Nat. Commun.* **2015**, *6*, 6142.
(29) Yin, W.-J.; Yan, Y.; Wei, S.-H. *J. Phys. Chem. Lett.* **2014**, *5*, 3625−3631.

DOI: 10.1021/jacs.5b13254
J. Am. Chem. Soc. 2016, 138, 5028−5035